Time-varying stimuli that prolong IKK activation promote nuclear remodeling and mechanistic switching of NF-κB dynamics

Authors

Steven W. Smeal[1], Chaitanya S. Mokashi[1,2], A. Hyun Kim[1], P. Murdo Chiknas[1], Robin E. C. Lee[1,3,†]

Affiliations

[1]Department of Computational and Systems Biology, School of Medicine, University of Pittsburgh, Pittsburgh, PA 15213, USA

[2]current address Altos Labs, Redwood City, CA, 94065, USA

[3]Center for Systems Immunology, School of Medicine, University of Pittsburgh, Pittsburgh, PA 15213, USA

Other footnotes

[†]Corresponding Author: robinlee@pitt.edu

Abstract

Temporal properties of molecules within signaling networks, such as sub-cellular changes in protein abundance, encode information that mediate cellular responses to stimuli. How dynamic signals relay and process information is a critical gap in understanding cellular behaviors. In this work, we investigate transmission of information about changing extracellular cytokine concentrations from receptor-level supramolecular assemblies of IκB kinases (IKK) downstream to the nuclear factor κB (NF-κB) transcription factor (TF). In a custom robot-controlled microfluidic cell culture, we simultaneously measure input-output (I/O) encoding of IKK-NF-κB in dual fluorescent-reporter cells. When compared with single cytokine pulses, dose-conserving pulse trains prolong IKK assemblies and lead to disproportionately enhanced retention of nuclear NF-κB. Using particle swarm optimization, we demonstrate that a mechanistic model does not recapitulate this emergent property. By contrast, invoking mechanisms for NF-κB-dependent chromatin remodeling to the model recapitulates experiments, showing how temporal dosing that prolongs IKK assemblies facilitates switching to permissive chromatin that sequesters nuclear NF-κB. Remarkably, using simulations to resolve single-cell receptor data accurately predicts same-cell NF-κB time courses for more than 80% of our single cell trajectories. Our data and simulations therefore suggest that cell-to-cell heterogeneity in cytokine responses are predominantly due to mechanisms at the level receptor-associated protein complexes.

Introduction

The typical body of an adult human has 10s of trillions of cells[1], and in some cases, individual cell behaviors can affect the entire organism. When cells are exposed to different biologic cues in their microenvironment, such as inflammatory cytokines, they activate dynamic signal transduction networks that mediate vital cell fate decisions. Deregulation of these networks contributes to a panoply of autoimmune diseases and cancers[2-4]. Variability and nonlinearity are typical characteristics of cellular signal transduction that limit our understanding of healthy and diseased cell behaviors and decisions processes. Variability arises from intrinsic and extrinsic sources of biochemical noise associated with stochastic molecular interactions that impact transcription rates, protein expression, among other biological processes[5-8]. Meanwhile, nonlinearity emerges due to complex biomolecular networks that include a host of feedback and feedforward loops. Adding to this complexity, the extracellular environment is dynamic, and cells are constantly exposed to multiple signaling molecules with changing concentrations. The combined effects of variability, nonlinearity, and dynamic input signals contribute to versatility of signaling pathways to regulate a wide range of responses. Therefore, experiments that combine single cell dynamics with computational modeling are important to reveal the capabilities of signaling systems and understand their emergent properties[9].

When inflammatory cytokines in the extracellular milieu activate transmembrane cytokine receptors, clustered receptors recruit cytoplasmic adaptors and enzymes to form a supramolecular protein assembly near the plasma membrane[10,11]. As the assembly matures, polyubiquitin scaffolds form around the protein core. A hallmark of cytokine

responses is recruitment-based activation of IKK kinase complexes to assemblies through the ubiquitin binding domain of NEMO, the IKK regulatory subunit[12-15]. Using fluorescent protein (FP) fusions of NEMO, individual assemblies can be visualized by live-cell microscopy as diffraction-limited puncta near the plasma membrane[16,17]. The mature protein assembly is a signal integration hub that activates IKK to coordinate downstream inflammation-driven NF-κB signaling. Although the supramolecular assemblies, referred to as 'complex I' (CI)[10,11], were first characterized for responses to tumor necrosis factor (TNF), interleukin-1ß (IL-1) and other cytokines produce CI-like assemblies with cytokine-specific receptors and adaptor proteins. CI and CI-like assemblies are reliant on different combinations of ubiquitin chain scaffolds[15,16]. However, all regulate IKK activation via induced proximity of IKK with other signaling mediators that reside on the assembly[18]. For simplicity, we refer to the family of CI and CI-like assemblies simply as 'CI'.

IKK activity following induction of CI promotes degradation of NF-κB inhibitor proteins (IκB) in the cytoplasm, and nuclear accumulation of NF-κB transcription factors[19]. Temporal properties of NF-κB in the nucleus encodes a dynamic transcriptional signal, regulating diverse gene expression programs that promote cell survival and propagate inflammatory signals. Live-cell tracking of FP fusions of the RelA subunit of NF-κB have provided instrumental data to understand and model transcriptional mechanisms and emergent properties that place the NF-κB pathway among exemplars of dynamical biological systems[20-22]. Key to these discoveries are negative feedback mediators, particularly IκBα, that are transcriptionally regulated by NF-κB. Following NF-κB activation, newly synthesized IκBα promotes nuclear export and cytoplasmic sequestration of NF-κB, restoring its baseline

cytoplasmic localization. Combined experiments and models have revealed mechanisms for dynamical regulation of nuclear NF-κB and transcriptional feedback; however, we have limited understanding of how information from dynamic extracellular signals is encoded and decoded within cells by the IKK-NF-κB signaling axis.

Typically, cellular signaling pathways have been studied using dose-response approaches that expose cells to continuous and unchanging extracellular stimuli. While responses to static concentrations provide a foundational readout for investigating cell behaviors, they are neither comparable to the dynamic signals observed *in vivo* nor sufficient to fully probe the versatility of cellular responses. We and others have recently shown that dynamic cell cultures can be achieved using PDMS- or acrylic-based microfluidic flow devices that vary with trade-offs between complexity, precision, and multiplex capabilities[23-26]. In most cases, single cell studies of signal transduction in dynamic microenvironments have revealed unexpected emergent properties that have inspired significant refinement of models that aim to predict and understand the underlying biological circuits[27-31].

In this work, we investigate IL-1 induced signaling in U2OS osteosarcoma cells to understand how information for time-varying extracellular cytokines is encoded within cells. The dual reporter cells were CRISPR-modified for endogenous FP fusions to observe active receptor complexes through supramolecular assemblies of EGFP-NEMO, the regulatory IKK subunit, and downstream dynamics of an mCherry-fusion of the NF-κB RelA subunit. Using live-cell imaging in a custom robot-controlled microfluidic cell culture system, we simultaneously measure upstream and downstream reporters in single cells exposed to dynamic stimuli. By observing I/O encoding of IKK-NF-κB signals and comparing cells

exposed to a single cytokine pulse with varied duration, we show monotonicity between the aggregate of activated receptor complexes and downstream TF dynamics. This result is consistent with our previous investigation of cells exposed continuously to static cytokine concentrations[17]. Remarkably, monotonicity of I/O encoding breaks down when cells are exposed to a series of short cytokine pulses. We observe that dynamic TF responses to pulse trains are significantly greater than expected from a single pulse, even when pulse trains are compared to a bolus of a larger overall cytokine dose. Enhanced TF responses to a cytokine pulse train can be attributed to marked alteration of nuclear export dynamics of NF-κB, transitioning from first-order to sustained zero-order kinetics in cells where activated receptor complexes persists for longer than 80 minutes. Using particle swarm optimization, we demonstrate that a mechanistic model does not recapitulate this emergent property of the IKK-NF-κB signaling axis and fails to switch to zero-order kinetics in response to a pulse train. By contrast, adding mechanisms for DNA binding and NF-κB-dependent chromatin remodeling, the resulting models recapitulate all the experimental findings. Our model suggests that temporal dosing that prolongs IKK activation facilitates pseudo-zero-order switching by two coupled mechanisms that prolong nuclear NF-κB retention without requiring persistent or saturating conditions: i) by promoting permissive chromatin states that expose new NF-κB binding sites; and consequently ii), by limiting the concentration of free nuclear NF-κB available to regulate expression of negative feedback mediators. Furthermore, simulations using the calibrated model to resolve experimental CI time courses from a complete set of single-cell validation data that were not used during optimization, accurately predicts same cell NF-κB responses for over 80% of single cell time

138 courses. Together, our results demonstrate that when overall cytokine dosage is limited,
139 temporal stimuli can encode distinct cellular behaviors, and that cell-to-cell variability in
140 cytokine responses is largely accounted for by variability of receptor-level mechanisms.

Results

IL-1 pulse duration produces a monotonic correlation between same-cell IKK and NF-κB responses

We previously developed a CRISPR-modified U2OS cell line that co-express FP fusions of NEMO (EGFP-NEMO) and RelA (mCh-RelA) from their endogenous loci. These dual-reporter cells were used to investigate the IKK-NF-kB signaling axis in cells exposed to continuous stimuli[17]. By simultaneously measuring time courses of fluorescence intensity for supramolecular assemblies of EGFP-NEMO as a reporter for CI and nuclear NF-kB in the same cell, these studies revealed fundamental aspects of signal encoding in the pathway. We reported that extracellular cytokine concentrations control the numbers and timing of formation for CI assemblies. Experiments that tracked EGFP-NEMO at individual CI assemblies revealed that fluorescence intensity time-courses of single puncta are invariant between different cytokine concentrations. Further experiments revealed cytokine-specific encoding, where a quantized number of EGFP-NEMO molecules is recruited at each CI structure. Here, TNF-induced receptor assemblies are shorter-lived and recruit approximately 30% the peak amount of EGFP-NEMO when compared with brighter and longer-lived IL-1-induced assemblies. Finally, we observed that activity from CI puncta is pooled for downstream signal transmission where the aggregate area under the curve (AUC) of CI puncta numbers is a strong same-cell predictor of the AUC nuclear NF-kB response.

Our previous results helped define the rules of signal encoding in terms of cytokine-specificity and static cytokine concentrations. However, these experiments did not investigate the orthogonal axis of how time-varying patterns of cytokines influence IKK-NF-

κB signaling. We therefore set out to probe the pathway by first measuring the dynamics of IKK and NF-κB responses as a function of cytokine pulse duration. To generate cytokine pulses while simultaneously performing high magnification single-complex imaging, we leveraged a recently developed dynamic stimulation system (DSS). The DSS consists of a custom robotic gravity pump controller that coordinates laminar fluid streams in a paired microfluidic cell culture device[24]. The microfluidic device was simplified from the previous DSS instrumentation as a two-inlet cell culture chamber (Fig. 1a, Supplementary Fig. 1, and Supplementary File 1). Here, one inlet is attached to a fluid reservoir with a mixture of cytokine, indicator dye, and cell culture medium, and to the other, a reservoir with medium only. Using the gravity pump to vertically relocate the fluid reservoirs generates hydrostatic pressure differentials at the inlets of the microfluidic device and positions the laminar cytokine-containing stream over the cells within (Fig. 1b). By varying the relative heights of the cytokine-containing and medium-only reservoirs, the system can be used to generate pulses in the experimental region of the cell culture device (orange boxes, Fig. 1b). In principle, the automated system described here operates like a manually controlled system we described previously[23], but with enhanced precision, reproducibility, and constant flow rates[24].

Using our dual-reporter cell line, we investigated the same-cell dynamics of NEMO assemblies and NF-κB nuclear translocation in a microfluidic device. We focused on cellular responses to 10ng/mL of IL-1, a non-saturating cytokine concentration that produces vibrant NEMO assemblies and unambiguous nuclear NF-κB responses[17]. Consistent with our previous results, dual-reporter cells in the device showed transient localization of EGFP-

NEMO to CI-like complexes, peaking in numbers by approximately 20 minutes, and robust nuclear translocation of mCh-RelA (Fig. 1c, and Supplementary Movie 1). Next, we measured single cell time-courses of EGFP-NEMO puncta and nuclear mCh-RelA in response to a single IL-1 pulse across a range of durations. Previously, we showed that time-integrated AUCs for trajectories of NEMO spot numbers and nuclear RelA fold change are scalar descriptors of single cell time courses that encode the most information about cytokine concentration[32,33]. Consistent with these results, AUCs of EGFP-NEMO spot numbers and nuclear mCh-RelA in single cells show increasing responsiveness with pulse duration and form a strongly monotonic continuum of same-cell correlations (Fig. 1d-f).

Previous works have shown that mammalian cell lines may follow an 'area-rule', where the fraction of responsive cells and overall NF-kB activation strength is proportional to the product of concentration and duration of cytokine stimulation[23,34]. Our current results are consistent with the 'area-rule', showing that information about extracellular pulse duration is also well determined when observed upstream via EGFP-NEMO puncta that provide an estimate for CI activation. Next, we asked if the area rule remains true for increasingly complex patterns of dynamic cytokine stimulation.

Cytokine pulse trains produce significantly greater NF-kB responses than expected from a single pulse

Cytokines typically have short half-lives *in vivo*, particularly for TNF and IL-1 that are rapidly cleared from the bloodstream within minutes[35-37]. Since inflammatory secretions in the vicinity of activated immune cells are also likely to be concentration and duration limited,

with localized depletion effects[38], cells may experience cytokines as a more rapid series of short pulses. Pulses of inflammatory cytokines have been shown to selectively regulate long lasting transcriptional programs. For example, in neuroblastoma cells, a single 5-minute pulse of TNF can initiate transcription of NF-kB-regulated early response genes that persist for hours, but not late response genes that require either constant or repeat cytokine stimulation[21]. We therefore asked whether a succession of short cytokine pulses in the extracellular milieu is encoded distinctly by the IKK-NF-kB axis, or if responses to a pulse train follows an 'area rule' equivalent to a single bolus of same overall dose.

We compared cellular responses between a single 6-minute pulse that produces an intermediate response strength (Fig. 1c and d), and multiple shorter pulses with the same cumulative IL-1 exposure but spread out in time. We partitioned a single 6-minute pulse equally into either two, three or four short pulses, and compared inter-pulse gap durations between 5 and 20 minutes (Fig. 2 and Supplementary Fig. 2). In comparison with a single 6-minute pulse, time-courses for NEMO puncta numbers in response to pulse trains showed lower peak values and longer spot persistence (Fig. 2a). Although in some pulse train conditions there was a subtle overall increase in AUC of NEMO puncta, these values typically did not reach significance and remained smaller than exposure to a larger single 15-minute pulse (Fig. 2 and Supplementary Fig. 2). Remarkably, despite only subtle and often non-significant increases in the AUC of IKK responses, many of the pulse-train conditions showed significant increases in the AUC of nuclear mCh-RelA time-courses (Fig. 2B). Even though pulse trains produced comparable peak amounts of nuclear RelA with similar timing to a dose-conserving single bolus, contributing to the stronger NF-kB AUC response was

markedly slower nuclear export. Nuclear export of NF-kB following a pulse train appeared almost linear, following zero-order kinetics. Nuclear export of RelA in response to a pulse train contrasts with most single pulse responses less than 30 minutes, which exhibit exponential nuclear export, as expected from first- and higher-order biomolecular reactions (Fig. 2 and Supplementary Movie 2). The enhancement effect of linear nuclear RelA export is exemplified by the condition with four 1.5-minute pulses of IL-1 separated by a 5-minute gap (4x1.5), which showed a greater than 2-fold increase in overall AUC. The nuclear RelA response strength for the 4x1.5 condition even surpassed responses to a 15-minute pulse despite the former having less than half the total cytokine exposure (Fig. 2B and Supplementary Movie 3). Finally, monotonicity of same-cell correlations between AUCs of NEMO spots and nuclear RelA was disrupted for pulse train conditions (Fig. 2C).

The unexpected increase in the response strength of nuclear RelA to a pulse train is an emergent property of the signaling pathway. We next asked whether the emergent property is specific to cytokine or cell type and found that strongly TNF-responsive KYM-1 rhabdomyosarcoma cells that express FP-RelA[23,33] show similarly enhanced responses to TNF pulse trains (Supplementary Fig. 3). Notably, some pulse train conditions diminish the emergent property effect. For example, conditions with fewer pulse numbers and longer inter-pulse gap lengths in the order of 10-20 minutes tend to have weaker nuclear RelA responses for both cell types and both cytokines (Supplementary Figs. 2 and 3). Together, these results suggest that cells can bypass the area rule in response to dynamic milieus and encode more information through CI assemblies than is represented by the scalar AUC of NEMO puncta.

Stimulation patterns that prolong NEMO puncta shifts the mechanism of NF-kB nuclear export

Since the AUC of NEMO puncta could not explain enhanced nuclear NF-kB in response to a pulse train, we asked if other quantitative features of EGFP-NEMO single cell time courses reflect the emergent property. When temporal features were quantified from NEMO time courses, distributions for both the timing of maximal (t_{max}) and time to adaptation (t_{adapt}) of NEMO spot numbers showed trends like the AUC of nuclear RelA (Fig. 3a-c).

Next, we set out to establish quantitative features of EGFP-NEMO that correlate with features of nuclear RelA. Because the maximum of nuclear RelA fold change did not show a strong trend between pulse-trains and dose-conserving single-pulses, we focused on scoring rates of nuclear RelA export (Fig. 3d and Supplementary Fig. 4a). As mentioned earlier, we visually observed that dynamics for nuclear RelA export appeared to switch from a first order to a pseudo-zero-order reaction (Figs. 2a and 3d) in response to a pulse train. To quantify this observation, single-cell nuclear RelA export dynamics were fitted to two models that represent zero-order and first-order kinetics (Supplementary Fig. 4b; and see methods). In the results, increasingly positive scores indicate a progressively stronger zero-order exit rate, while negative values correspond to first-order exit rates. We observed that single 6-minute and 15-minute pulse shows strong first-order dynamics and the responses to pulse trains showed strong zero-order kinetics (Supplementary Figs. 1c, d and 4c). Finally, we correlated features of EGFP-NEMO against the nuclear RelA export order score. Although t_{max} of NEMO only correlated weakly, by contrast, t_{adapt} of NEMO showed a strong monotonic

correlation with the nuclear RelA exit rate score (Fig. 3e, f). Based on our data, stimulation profiles that prolong CI assemblies beyond 80 minutes shift the nuclear export rate of RelA towards a pseudo-zero-order process and thus enhance the AUC of the nuclear NF-kB response.

A model with chromatin remodeling recapitulates the emergent property and nuclear NF-kB export

Mechanistic models provide mathematical representations of biological systems, enabling researchers to test hypotheses and synthesize their understanding of system-level behaviors. Ordinary differential equation-based models of the NF-kB transcriptional system have been deeply informative. Previous models parameterized to quantitative assays and single cell data have been used to investigate nuclear translocation dynamics of NF-κB, emphasizing negative feedbacks from IκB isoforms[39] and A20[21], as well as mechanisms for fold change detection (called D2FC, derived from previous models)[32]. Each of these models has been built upon their predecessors to answer different questions. However, none of the models have been parameterized to single receptor-complex data and dynamic stimuli.

To explore the possible biological mechanisms that contribute to zero-order switching and enhanced nuclear RelA retention in response to a pulse train, we first asked if the D2FC model directly recapitulates experiments. Since we have a compendium of single cell data from dual-reporter cell lines, we modified the model to activate IKK directly from experimental time courses of EGFP-NEMO puncta and simulate nuclear NF-κB responses (Fig. 4a). We first tested the previously published parameterization of the D2FC model, using

a fitted scaling parameter to interface experimental data for EGFP-NEMO puncta that produces a best fit simulated NF-κB response (see methods). Although the naive D2FC model replicates the AUC of NF-κB for responses to a single pulse, the model results did not show increased AUC of nuclear NF-κB nor switching to zero-order export mechanisms when simulations were run using EGFP-NEMO pulse-train data as inputs (Supplementary Fig. 5).

Next, we tested if the topology of the D2FC model can reproduce the emergent property using parameter optimization. Particle swarm optimization (PSO) is a bio-inspired algorithm that searches parameter space for candidate solutions, using an objective function to measure the quality of fit for each[40]. Implementations of PSO often identify nearly global optimal parameterizations in high-dimensional and rugged objective landscapes. To decrease the computational time, we considered a minimal dataset of 4 experimental conditions that manifest the emergent property (consisting of control, 1x6min, 4x1.5min, and 1x30min pulse data; Fig. 4a top panel). Subsequently, we used PSO to simulate responses to the average of EGFP-NEMO time-courses from each condition, using the average of nuclear mCh-RelA for each condition as the objective function (Fig. 4A). PSO was repeated 500 times to generate parameter sets that sample the model's best fits to data. For the 500 parameter sets, we performed post-hoc analysis to evaluate three error criteria for each: i) error in producing a nearly 2-fold increase in the AUC of nuclear NF-κB comparing 1x6min and 4x1.5min conditions, referred to as the 'emergent property' score; ii) the average sum squared error (<SSE>) of fits to the 4 training conditions; and, (iii) the SSE of fits to validation data consisting of 5 mean experimental conditions that were not used for PSO (Fig. 4b). Remarkably, each of the optimized D2FC models had high error scores across

317 evaluation criteria (Fig. 4b), failing to recapitulate the system's emergent property
318 (Supplementary Fig. 5c). Taken together, the results suggest that the topology of the D2FC is
319 missing critical circuitry that is necessary to explain the experimental observations.

320 Pseudo-zero-order processes are unusual behaviors in biological systems because
321 they appear to be independent of reactant concentrations. Typically, zero-order kinetics
322 result from systems where one of the reactants is greatly limited or scaffolded into a lower
323 reactivity state. Since NF-κB is well established as a transcription factor, we hypothesized
324 that NF-κB binding to broadly to DNA[41-45] may be an essential mechanism that is not explicit
325 in the D2FC model. Furthermore, there is a growing body of literature that characterizes
326 chromatin remodeling capabilities of NF-kB. For example, NF-kB can bind to assembled
327 nucleosomes and flanking DNA, contributing to DNA unwrapping and nucleosome
328 displacement[46,47]. Chromatin reorganization was found to decode the duration of nuclear
329 NF-kB, where prolonged nuclear TF contributes to stimulus- and gene-specific transcription
330 initiation by progressively revealing promoter sequences that are otherwise closed in basal
331 conditions[48]. More recently, prolonged non-oscillatory nuclear NF-kB was shown to cause
332 cytokine-inducible alterations to chromatin accessibility near NF-kB binding sequences,
333 activation of latent enhancers, and epigenetic reprogramming[22]. Therefore, additional
334 mechanisms were added to the model, to include NF-kB binding to DNA and chromatin
335 remodeling that reveals additional NF-kB binding sites via mechanisms akin to pioneering[49]
336 (see methods). The modified D2FC model with chromatin remodeling is referred to as D2FC-
337 squared ($D2FC^2$) henceforth (see methods, Supplementary Tables 1 and 2).

338 Using PSO, we again sampled 500 parameter sets with the $D2FC^2$ architecture. The

339 D2FC^2 model produced high quality fits, significantly reducing scores of the 3 error criteria
340 (Fig. 4B). Parameterization sets of the D2FC^2 from PSO showed that the approach effectively
341 explored the prior distribution of acceptable parameters, and the top 10 scoring models
342 were able to achieve a similar quality of results despite being derived from distinct
343 combinations of parameters (Fig. 4B, and Supplementary Fig. 6). Taken together, the
344 topology of D2FC^2 enables the model to recapitulate the average behaviors of all
345 experimental conditions, with robustness to variation of parameters.
346
347 **A model with chromatin reorganization accurately predicts single cell responses and**
348 **experiments**
349 Training and validation simulations with the D2FC^2 model used averages of experimental
350 single cell time courses for each condition, both as inputs to simulations and to evaluate the
351 quality of fits. We next asked whether the D2FC^2 accurately predicts single-cell dynamics.
352 Using the 3 error criteria to rank the models, the top-performing parameter set in the D2FC^2
353 was selected for further analysis (Fig. 4b, red asterisk). Single-cell EGFP-NEMO time-
354 courses from all the single pulse and pulse train conditions were as inputs to simulate
355 nuclear NF-kB responses. Visually, simulated single-cell time courses of nuclear NF-kB
356 appeared like experiments, showing both first-order and zero-order nuclear export kinetics
357 appropriate to each condition (Fig. 5a). AUCs of simulated nuclear NF-kB to single pulse
358 conditions showed dose-responsiveness, and consistent with expectations based on error
359 scores following PSO, D2FC^2 simulations for pulse trains recapitulated the emergent
360 property (Fig. 5b and c). Furthermore, interquartile ranges of boxplots were similar when

comparing experiments and simulations, suggesting that cell-to-cell variability at the level of CI dynamics contributes significantly to variability of nuclear NF-kB dynamics observed in single-cell experiments.

Following, we moved away from population average data and evaluated the quality for single cell fits by measuring the SSE between experimental nuclear RelA trajectories and simulated NF-kB dynamics. An elbow plot was used to define the error threshold to classify low- and high-quality fits, and a stricter threshold was applied to define a third class of 'excellent fits' where experiment and simulations overlap almost perfectly (Supplementary Fig. 7). When compared between experimental conditions, performance of the D2FC^2 was consistent with most single cells showing high- and excellent-quality fits (Fig. 5d, left). The single 15-minute pulse and the 3x2min were the conditions that showed the most low-quality fits; nevertheless, even these weakest conditions still achieved excellent or high-quality fits for approximately 70% of single cell trajectories. Comparing the top 10 D2FC^2 parameter sets, all recapitulate single pulse dose-responsiveness and the emergent property, as well as produce high-to-excellent predictions for over 80% of the single cell nuclear RelA trajectories aggregated across all conditions (Fig. 5d, right; see also Supplementary Table 3). These results demonstrate that many different parameterizations of the D2FC^2 architecture can robustly resolve single-cell EGFP-NEMO time courses and predict nuclear RelA responses across a heterogeneous population of cells.

Finally, we asked whether the D2FC^2 can predict the impact on nuclear RelA dynamics in the presence of a chromatin perturbation. Azacitidine is cytidine analog that incorporates into DNA and inhibits DNA-methyltransferase DNMT1, promoting

hypomethylation and chromatin relaxation over timescales of days[50]. To model the effects of azacytidine, the term representing basal DNA accessibility was increased and the model was allowed to adapt to a new steady state before resolving the average EGFP-NEMO time course for a 6-minute pulse. The simulations revealed two trends: first, that progressively relaxed chromatin leads to increased basal abundance nuclear RelA; second, that fold-change responses of nuclear RelA following cytokine stimulation are effectively reduced (Fig. 6a and b). To test these model predictions, cells were cultured in the presence of azacytidine for 3 or 6 days before exposure to a single 6-minute pulse of IL-1. Although 3 days of culture with azacytidine appeared like untreated control cells, 6-day samples were consistent with the model, showing significant enrichment of basal RelA prior to stimulation and suppressed nuclear RelA dynamics in response to IL-1 (Fig. 6c, d, and Supplementary Fig. 8). Thus, chromatin organization influences cytokine-induced temporal profiles of nuclear NF-kB.

Peak number and adaptation time of CI fine tunes chromatin permissiveness and nuclear NF-kB dynamics

Temporal profiles of IKK activity encode information about the abundance and type of inflammatory factors in the milieu, regulating nuclear NF-kB and stimulus-specific gene expression programs[17,51]. Our results here show that features of IKK at CI assemblies also encode information about temporal presentation of cytokines, such as their numbers and timing, that in succession regulate feedback pathways in the nucleus (Fig. 7a).

Based on single cell time courses of EGFP-NEMO from static cytokine

concentrations[17], single cytokine pulses (Fig. 1), and cytokine pulse trains (Fig. 2), CI-encoding can be decomposed into a primary peak and a second slow-adapting distribution (Fig. 7b). We leveraged the D2FC[2] to systematically evaluate the impact of CI-encoding features on downstream signaling (Fig. 7c). First, we considered nuclear NF-kB fold change, which we showed previously to correlate strongly with NF-kB-regulated early response genes[32]. Here, maximal nuclear NF-kB correlates with peak CI numbers that saturate around 300, and adaptation time for the secondary distribution had negligible impact (Fig. 7c, top left). Comparing rates of nuclear NF-kB export showed a non-linear relationship with CI-encoding features. A primary peak of approximately 50 CI puncta and adaptation times of greater than 80 minutes were both strictly required for conversion of nuclear NF-kB export rates from a first order to pseudo-zero-order process (Fig. 7c, top right). Higher peak CI numbers required even longer adaptation times to achieve zero-order NF-kB export kinetics, possibly requiring greater CI persistence to compensate for stronger first-wave transcription negative feedback mediators, such as IkBα. Chromatin openness showed a similar pattern, requiring a minimum peak CI of nearly 100 puncta, and prolonged activation to increase overall permissiveness (Fig. 7c, bottom left). Even the highest peak CI numbers failed to enhance chromatin opening unless adaptation time also persisted for more than 60-80 minutes. Finally, since open chromatin reveals new NF-kB binding sites, both productive and non-productive in regulating gene transcription, we measured the fraction of free nuclear NF-kB as a function of chromatin status. Remarkably, even when concentrations of nuclear NF-kB are at their highest, permissive chromatin can deplete free nuclear NF-kB (Fig. 7c, bottom right). Therefore, despite high total concentrations of nuclear NF-kB, permissive

chromatin at later times may only leave trace amounts of free nuclear TF to interact with promoters of early response genes such as IkBα.

Studying I/O relationships in dual-reporter cells exposed to dynamic stimuli, while leveraging naturally occurring cell-to-cell variability, revealed features of CI encoding that regulate time profiles of nuclear NF-kB. Simulations with the D2FC[2] show that the primary peak of CI determines the fold change of nuclear NF-kB and the adaptation time facilitates switching towards more permissive chromatin states with additional NF-kB binding sites. Importantly, DNA-based sequestration of nuclear NF-kB is transient, and the model allows nascent IkBα polypeptides to interact with DNA-bound NF-kB to facilitate dissociation, as seen in experiments[52]. Together, our experiments and simulations suggest that the transition to a pseudo-zero-order export process results from the combined effect of sequestration and feedback depletion on early gene promoters.

Discussion:

On the surface of a human cell, the number of IL-1 and TNF receptors is relatively small, estimated in the range of hundreds to low thousands per cell[17,53]. Following cytokine stimulation, ligated receptors are rapidly internalized and degraded [54,55]. Therefore, a limited and depletable resource of surface receptors is available to encode information about the inflammatory milieu into the cell via CI assemblies. We reasoned that cytokine conditions that spread out a stimulus in time may encode different signals from tonic and saturating boluses that would rapidly deplete the available receptor pool. To this end, our result shows that temporal properties of IKK encode information about time-varying extracellular conditions that can be used by the cell in succession to regulate distinct temporal response patterns of nuclear NF-κB.

We used dynamic stimuli, dual-reporter cells, and computational models to investigate information encoding properties of the IKK-NF-κB signaling axis. Exposing dual-reporter cells to a single cytokine pulse revealed that the aggregate AUCs of IKK and nuclear NF-κB increase with the IL-1 pulse duration, forming a continuum of single cell I/O responses (Fig. 1f). In contrast, when a cytokine is presented as a series of short pulses, monotonicity of the aggregate I/O response is disrupted with cells showing disproportionately enhanced AUCs for nuclear NF-κB responses (Figs. 2 and 3). We determined that the aggregate AUC of IKK puncta is not sufficient to predict same-cell NF-κB responses to dynamically presented stimuli. Instead, orthogonal axes for peak numbers and adaptation times of CI were predicted to encode signals that enhance NF-κB responses by mechanisms that switch nuclear export from a first- to pseudo-zero-order process. Although both features are

important contributors, CI adaptation times where EGFP-NEMO puncta persist for around 80 minutes or longer define a threshold for conversion to zero-order kinetics. This observation is reminiscent of a previous computational prediction where a constant plateau of low-amplitude IKK activity following can mediate long-lasting nuclear NF-κB time profiles[51]. Nevertheless, experiments differ from these predictions because CI assemblies and IKK kinase assays in wild-type cells[16,17,51,56] show adaptation, typically within 60-90 minutes following exposure to TNF or IL-1. Based on our experiments and model results, we surmise that the tail of IKK activity that extends beyond 80 minutes is crucial to blunt the first wave of IκBα-mediated feedback, subsequently facilitating nuclear remodeling that supports zero-order export kinetics.

In contrast with experiments, and regardless of model parameterization, simulations with the D2FC model[32] to predict NF-κB responses did not show switching between first- and zero-order nuclear export kinetics, and the emergent property with enhanced response AUCs. The D2FC[2] modified the base model by invoking explicit DNA-binding and chromatin-remodeling mechanisms for NF-κB. These were selected because they reflect increasingly well-characterized mechanisms that can create reactant-limiting conditions necessary for a pseudo-zero-order process. To illustrate this point, NF-κB binds to hundreds of non-redundant sequences that are distributed with repetition throughout the human genome[43,57]. Early estimates predicted that there are significantly more binding sites in the genome than the ~10^5 NF-κB molecules in a typical mammalian cell[41]. Subsequently, tens of thousands of NF-κB binding sites have been observed in macrophages and B cells, as well as enrichment of NF-κB binding on the 5' end of genes or other non-promoter sequences[42,44,45]. More recent

results using genetic knockout of IkBα in mouse BMDMs showed prolonged nuclear NF-κB following TNF stimulation, along with disruption of nucleosomal histone-DNA interactions in the vicinity of NF-κB binding sites[22]. Since earlier studies did not use genetic or chemical perturbations that are necessary to produce prolonged nuclear NF-κB responses and chromatin reorganization in differentiated immune cells, they are likely to underestimate the breadth of NF-κB-DNA interactions. Taken together, there is a vast abundance of productive and non-productive NF-κB-DNA interactions that are basally accessible, and significantly more following chromatin reprogramming[48]. Incorporation of these roles in the D2FC^2 revealed that consequences of DNA-binding and chromatin are sufficient to switch nuclear NF-κB export to a pseudo-zero-order process. Consequently, our results also suggest that mechanisms associated with chromatin dynamics and epigenetic reprogramming are selected via dynamic stimuli that control the timing and numbers of CI. There is growing recognition of multi-hit immune signaling where cytotoxicity is additive over multiple sub-lethal interactions between immune and cancer cells[58,59]. With these observations, our results support that dynamic cytokine presentations, such as multi-hit pulses, may encode distinct messages to receiving subpopulations of non-immune cells, including cancers.

By using PSO to fit averaged experimental data from four conditions that embody the emergent property, families of model parameterizations were identified that successfully recapitulate experiments. As discussed earlier, the D2FC^2 model architecture was modified for chromatin permissiveness and DNA binding only, and did not invoke any additional molecular species or mechanisms. Simulations *in silico* further demonstrated capabilities of D2FC^2 to accurately predict single cell NF-κB responses from time courses of CI, validated

505 with a compendium of experimental trajectories from dual reporter cells. Given that there
506 were no single-cell data used during optimization, it was remarkable that a family of different
507 model parameterizations was found, each capable of accurately predicting same-cell NF-
508 κB responses from experimental EGFP-NEMO time profiles. The added mechanisms of
509 D2FC^2 are robust, allowing the resulting system to achieve consistent behavior without
510 requiring strict expression levels for all molecular species in the model that individually tend
511 to exhibit variability when measured in single cells. Taken together, low numbers for cytokine
512 receptors and stochasticity of their interactions are among the chief contributors to
513 heterogeneity between single cell NF-κB responses, which can be accurately predicted from
514 CI-level measurements.

515 Dynamics of nuclear NF-κB mount stimulus-specific adaptive responses through
516 selective regulation of gene expression programs, many of which cluster into early-, mid-,
517 and late-response categories[21,51,60]. Although late response genes are typically associated
518 with tonic and high-concentration inflammatory stimuli, this may not be strictly required.
519 Based on our experiments and model, we speculate that mid- and late-response genes can
520 arise from chromatin accessibility, and that certain temporal stimuli that distribute CI
521 numbers in time have the potential to reveal their promoters via chromatin remodeling.
522 However, follow-up studies to test this possibility will require further refinements to our
523 model. For example, the mechanism for chromatin remodeling in the D2FC^2 is likely to be an
524 oversimplification, lacking mechanisms for gene-specific promoter accessibility and other
525 DNA-binding proteins such as AP-1 that remodel chromatin in response to inflammation[61,62].
526 Similarly, theoretical IKK distributions studied in the model may be difficult to achieve

527 experimentally, and another layer of detail is necessary to accurately predict the distribution
528 of peak numbers and timing from complex environmental stimuli. Nevertheless, we expect
529 that forthcoming models will explicitly model CI puncta and gene-specific promoters
530 relative to chromatin. Through a comprehensive model, we will understand how basal
531 conditions of different cell types encode and decode certain cytokine responses, and how
532 complex environments can select gene expression programs using CI and IKK as signaling
533 hubs.

534 In summary, our results demonstrate that the number and timing of CI assemblies
535 encode information about time-varying stimuli in the extracellular milieu. With limited
536 numbers of surface receptors to nucleate CI assemblies, extracellular conditions that
537 prolong the adaptation time of CI disproportionately enhance the aggregate NF-κB response.
538 These observations are recapitulated in a model of NF-κB signaling by invoking mechanisms
539 for DNA-binding and chromatin reorganization. The resulting system reveals how IKK-
540 encoding of dynamic environmental conditions distinctly coordinate a range of potential NF-
541 κB responses through systems feedback and chromatin remodeling.

Methods

Cell Culture

CRISPR-modified U2OS cells expressing N-terminal fusions of EGFP-NEMO and mCherry-RelA from their endogenous loci[17], as well as KYM-1 cells stably expressing mVen-RelA, were cultured in McCoy's 5A and RPMI medium respectfully at 37°C in a humidified incubator with 5% CO_2. The medium was supplemented with 10% fetal bovine serum (FBS) (Corning), penicillin (100 U/mL), streptomycin (100 U/mL), and 0.2 mM L-glutamine (Invitrogen). Cells were routinely screened for mycoplasma contamination.

Live-cell imaging for pulse experiments in the microfluidic dynamical stimulation system

A custom microfluidic system, as previously described[24], was used for single and repeat pulse experiments. Briefly, two-inlet PDMS devices were fabricated from corresponding 3D-printed molds, sterilized by autoclaving, washed with ethanol, followed by PBS and subsequently incubated with a 0.002% (v/v) fibronectin solution in PBS for 24 hours at 37°C. U2OS double-CRISPR cells (~5×10^6 cells/mL) were seeded into the microfluidic devices and incubated for at least 24 hours.

On the day of the experiment, the microfluidic device was connected using Tygon tubing to fluid reservoirs on the gravity pump containing the appropriate treatments. FluoroBrite DMEM medium (Gibco, A18967-01) supplemented with 10% FBS (Corning), penicillin (100 U/mL), streptomycin (100 U/mL), and 0.2 mM L-glutamine was used during imaging. IL-1 and

564 TNF treatments were prepared with Alexa Fluor 647–conjugated BSA (0.0025% v/v of a 5
565 mg/mL stock; Invitrogen) to visualize the cytokine containing stream in the device.
566
567 Images of EGFP-NEMO were acquired every 4 minutes using FITC filters, with a z-stack of
568 eight images at 0.5-µm intervals, using 0.04-second exposure and 32% transmission.
569 Similarly, mCherry-RelA was imaged every 4 minutes using the Alexa A594 filters, with 0.1-
570 second exposure and 50% transmission. Alexa Fluor 647–conjugated BSA was imaged every
571 1 minute using the CY5 channel with 0.1-second exposure and 50% transmission. All images
572 were acquired in an environmentally controlled chamber (37°C, 5% CO_2) on a DeltaVision
573 Elite microscope equipped with a pco.edge sCMOS camera and an Insight solid-state
574 illumination module (GE Healthcare) at 60x LUCPLFLN oil objective.
575
576 **Treating cells with 5-azacitidine**
577 U2OS double-tagged cells were treated with 5 uM of azacitidine (Sigma Aldrich, A2385) while
578 growing in a 10 cm dish. Since azacitidine is reported to degrade rapidly in aqueous solutions
579 at room temperature, cells received fresh 5 uM azacitidine daily for 3 or 6 days before
580 imaging. The day before imaging, cells were seeded on a 96-well plate at 6,000 cells/well.
581 On the day of imaging, the media in the wells were replaced with FluoroBrite DMEM
582 supplemented with FBS, penicillin, streptomycin, and L-glutamine. A single 6-minute pulse
583 of IL-1 at 50 ng/mL was given to the cells. 50 ng/mL was chosen because it most resembled
584 the IKK profile of a single 6-minute pulse of IL-1 in a microfluidic chip. Cells were imaged to
585 measure the nuclear localization of mCherry-RelA for 3 hours, with 4 minutes intervals.

586

587 **Extracting EGFP-NEMO and mCherry-RelA time profiles from live-cell images**

588 As previously decribed[63,64], dNEMO software was used to detect and quantify EGFP-NEMO
589 spots. The spot detection threshold in dNEMO was set between 2.1 and 2.4, and only spots
590 present in at least two contiguous slices of the 3D images were considered valid. Individual
591 cells were manually segmented using dNEMO's keyframing function. The mCherry-RelA
592 nuclear intensity trajectories were quantified using custom python scripts. Briefly, the
593 custom scripts allowed to identify regions of background and the nucleus across all frames
594 by defining regions by a box. Nuclear NF-kB was determined by calculating the mean pixel
595 intensity of the nucleus by the mean background intensity of the frame. Each cell trajectory
596 was manually tracked across all images. To calculate the fold change, mCherry-RelA
597 trajectories were divided by the initial nuclear fluorescence at time zero. The area under the
598 fold-change curve was calculated by first subtracting by 1 and setting any negative values
599 equal to 0. The trapezoidal function in MATLAB was used to calculate the area under the
600 curve from the data.

601 $$NFkBFC\ AUC = trapz(\max(NFkBFC - 1,0))$$

602 Where NFKBFC represents the fold change nuclear NF-kB.

603

604 **Mechanistic modeling**

605 The mechanistic model of NF-kB activation through IKK, called D2FC, was used as
606 previously published[32]. Briefly, the mechanistic model contains the key events from IKK
607 activation, degradation of IkB due to IKK, NF-kB translocation to the nucleus, and the up-

608 regulation of IkB in the cell. To interface the single-cell measurements of IKK punctate
609 formation, the D2FC model was modified such that the activation of IKK from its neutral state
610 depended on the formation of IKK punctate structures. The rate of formation is:

611 $$IKK_n \rightarrow IKK$$

612 $$Rate = k_a * IKKSpots(t) * IKK_n$$

613 The parameter k_a was optimized to reduce the sum of the squared error of the training data
614 and represents the parametrization of D2FC.

615

616 The input, IKKSpots(t), consists of experimental trajectories obtained from live-cell imaging.
617 These trajectories were fitted to a sum of four Gaussians using MATLAB's fit function. To
618 ensure that the fitted curve started at zero, additional weight was placed on the initial value
619 during optimization. Finally, all simulated IKK trajectories were visually inspected to confirm
620 that they captured the basic trends observed in the experimental data.

621 $$IKK(t) = \sum_{i=1}^{4} a_i e^{\left[-\left(\frac{(x-b_i)}{c_i}\right)^2\right]}$$

622 The parameters for each single cell IKK trajectory and mean IKK trajectory can be found in
623 the ModeledIKKTrajectories.xlsx supplementary information.

624

625 The D2FC[2] model introduced an additional mechanism that was necessary to fit the
626 emergent property as described in the results. The new mechanisms involved NF-κB binding
627 and opening new DNA-binding sites in chromatin. This mechanism includes a new model
628 species, NFκBDNA, representing NF-κB bound to DNA. The binding rate of NF-κB to DNA is

629 influenced by cooperative effects, where the presence of already-bound NF-κB increases
630 the likelihood of additional NF-κB binding. This phenomenon reflects a so-called pioneering
631 effect[49] in which the binding of NF-κB facilitates chromatin relaxation, opening more binding
632 sites and enhancing NF-κB recruitment where Ps_0 represents the basal nuclear openness
633 and was fixed to a value of 1:

634 $$NFkB \rightarrow NFkBDNA$$

635 $$Rate = ka1d * DCoop * NPio$$

636

637 $$DCoop = \frac{\left(\frac{NFkB}{\mathrm{kdNFKB}}\right)^{h2}}{1 + \left(\frac{NFkB}{\mathrm{kdNFKB}}\right)^{h2}}$$

638

639 $$NPio = Ps_0 + Ps * \frac{\left(\frac{NFkBDNA}{KDNA}\right)^{h3}}{1 + \left(\frac{NFkBDNA}{KDNA}\right)^{h3}}$$

640

641 NF-κB can dissociate from DNA either through direct binding of nuclear IκBα or via a basal
642 rate of dissociation. The two methods follow basic mass action kinetics

643 $$IkBa + NFkBDNA \rightarrow IkBaNFkB$$

644 $$Rate = ka2a * [N.IkBa] * [N.NFkBDNA]$$

645

646 $$NFkBDNA \rightarrow NFkB$$

647 $$Rate = kd1d * [NFkBDNA]$$

648

Emergent property score

The emergent property score was calculated by first simulating nuclear RelA trajectories for each of the single cell trajectories of the single 6, single 15, and four 1.5-minute pulses. Since Fig. 2 showed an increase in the median AUC of nuclear RelA (fold change) between the single 6-minute and 4x1.5-minute pulses and between the single 6-minute pulse and single 15-minute pulse, the emergent property score was defined as follows:

$$Emergent\ Property\ Score = abs\left(\frac{med(AUC_{4x1.5})}{med(AUC_{1x6})} - \frac{med(\widehat{AUC_{4x1.5}}(\theta))}{med(\widehat{AUC_{1x16}}(\theta))}\right) + abs\left(\frac{med(AUC_{1x15})}{med(AUC_{1x6})} - \frac{med(\widehat{AUC_{1x15}}(\theta))}{med(\widehat{AUC_{1x16}}(\theta))}\right)$$

Where $\widehat{\mathrm{AUC}_{1\mathrm{x}6}}(\theta)$, $\widehat{\mathrm{AUC}_{1\mathrm{x}15}}(\theta)$, $\widehat{\mathrm{AUC}_{4\mathrm{x}1.5}}(\theta)$ represents the data set of single-cell predictions for the parameter set θ for the AUC of the nuclear RelA (fold change) for the 1x6, 1x15, and 4x1.5-minute pulses. AUC_{1x6}, AUC_{1x15}, and $\mathrm{AUC}_{4x1.5}$ represent the area under the curve for the experimental single cell trajectories.

Model simulations

D2FC and D2FC^2 were built using MATLAB 2023a. Associated code is available through the supplement (Supplementary Files 2) and the following repository (https://github.com/recleelab/D2FCSquared/) . SimBiology was used to generate ordinary differential equations from the reaction rates. Models were simulated for 10 days without cytokine stimulation to ensure a steady state was reached. Then the IKK profile corresponding to the appropriate dose was simulated to get the simulated results. Particle swarm optimization from MATLAB's Global optimization toolbox was used to optimize the parameter set to fit the average results from four scenarios used for fitting which included

the control, 1x6 minute pulse, 1x30-minute pulse, and 4x1.5-minute pulse of IL-1. The global optimization attempted to minimize the following equation where $y_{i,t}$ is the experimental measurement for scenario i at time = t, and $\hat{y}_{i,t}(\theta)$ is the model estimate for parameter set θ:

$$J(\theta) = \sum_i \sum_t \left(y_{i,t} - \hat{y}_{i,t}(\theta)\right)^2 + NFkB_{Herusitic}(\theta)$$

Where:

$$NFkB_{Herusitic}(\theta) = \begin{cases} 0 & if\ 0.01 < R_{\frac{nuc}{cyt}} < 0.3 \\ 100 & if\ R_{\frac{nuc}{cyt}} < 0.01 \\ 5 * R_{\frac{nuc}{cyt}} & if\ R_{\frac{nuc}{cyt}} > 0.3 \end{cases}$$

The $NFkB_{Herusitic}$ was designed to ensure proposed parameters had a basal nuclear NF-kB described as the ratio of NF-kB in the nucleus to cytoplasm ($R_{\frac{nuc}{cyt}}$) within experimental expectations. Model values going below the lower limit were strongly penalized whereas models above were penalized proportional to ratio. The heuristic was set up to significantly penalize the overall optimization score if the basal nuclear NF-kB conditions were not met.

Particle swarm optimization was run with a swarm size of 100 particles and ceased after 20 consecutive iterations to prevent stalling, where the system could not achieve a reduction in the optimization score. Parameter values were optimized in $\log_{10}$ format to help the optimizer explore the full parameter space across multiple orders of magnitude. The prior distribution of parameters ranges for optimization were carefully selected to represent biophysically relevant ranges around each parameter in the D2FC model (Supplementary table 4).

690

691 **Quantification of zero- vs. first-order nuclear export kinetics**

692 Single-cell trajectories of nuclear NF-kB fold change were classified as having first- or zero-
693 order nuclear export kinetics by fitting two models to data at the point of nuclear NF-kB
694 exiting the nucleus. A linear model was fit between the point of decay and the last data point.
695 The first order decay model was fitted by setting N_0 to the value of decay and finding the k
696 value that minimized the sum of squared error. To avoid parameters for the first order decay
697 rate that are linear, a minimum parameter exponential rate constant of k was set to 0.0167
698 min^{-1} which represents a first order decay rate where approximately 95% of the nuclear Rela
699 would exit the nucleus within 180 minutes. Defining a maximum value was essential to
700 create a single metric for differentiating first and zero order decay rates.

701

702 Zero-Order Decay Model:

703 $$y = m * t + b$$

704

705 First-Order Decay model:

706 $$y(t) = N_0 * e^{-k*t}$$

707

708 For each single-cell trajectory, the time point of nuclear NF-kB exit rate was identified and
709 the first and zero order models were fit to the data, only considering points after NF-kB
710 started to exit the nucleus. The sum of squared error (SSE) was determined for both models
711 and the nuclear RelA exit rate score is calculated to be the difference between the $SSE_{Zero} -$

SSE_{First}. Positive values indicate zero-order and negative values indicate first-order nuclear export kinetics.

Benchmarking the quality of the single cell predictions

Single-cell IKK trajectories were used as input for the model to generate predictions for each cell. The sum of squared errors (SSE) was calculated for each of the 194 single-cell model predictions to assess their accuracy. To classify the quality of these predictions, we established thresholds for 'excellent,' 'high,' and 'poor' fits. The threshold for 'high' fits was determined using an elbow plot. This was done by gradually increasing the threshold and counting the number of unacceptable fits (see Supplementary Fig. 7). To identify the elbow point, we first drew a line connecting the first and last points on the plot. We then measured the perpendicular distances from each point on the elbow plot to this line. The point with the maximum distance from the line was selected as the elbow point, which defined the optimal threshold for high-quality fits. To further classify the single cell trajectories, we divided the single cell trajectories between simulations that were considered excellent (which was defined as half of the elbow point) and high-quality fits.

SimBiology model

A mechanistic model was constructed using SimBiology (MATLAB) by employing command-line tools within an m-file, rather than the graphical interface. This approach enhanced flexibility and automation in model development and simulation. SimBiology was used as a

tool to automate the process of converting from reaction rate equations to a set of ordinary differential equations (ODE).

Simulated CI Trajectories

Simulated CI trajectories were generated by first creating an zeros array with one value set to 1, representing the peak time. The array had a length of 46, matching the number of timepoints in our time-lapse imaging. The peak was positioned at 28 (index position 7) minutes, and a linear interpolation filled in the values between timepoints 0–28 and 28 to a variable adaptation time, resulting in trajectories with a triangular shape. To aid downstream fitting to Gaussian equations, a rolling average with a window of 3 was applied to smooth the trajectory. The smoothed CI trajectories were then fit to the sum of four Gaussian equations, for simulation in the model. To ensure simulation started at zero, additional weight was added to t=0 to the optimization function. With the method, we can precisely control the peak height, peak time, and adaptation time for the CI trajectories.

Simulation of Chromatin Opening

Chromatin opening to simulate azacitidine treatment was done by increasing the basal chromatin openness parameter, Ps_0. To estimate the effect of chromatin permissiveness on the fraction of free NF-κB, a sub-model was constructed that included only the binding and unbinding of NF-κB to DNA. In this model, only free and bound NF-κB were dynamic, while all other species, specifically IκBα, were held constant at the steady state value before CI formation. The rate of NF-κB binding to DNA was determined by the equation:

$$Rate_{Binding} = ka1d * DCoop * NPio_{const} * [N.NFkB]$$

where $NPio_{const}$ was held constant during the simulation but varied for generating the heatmap in Fig. 7C (bottom-right). The rate of NF-κB unbinding from DNA was influenced by both the basal dissociation rate and binding to IκBα. IκBα was set to a constant value, equal to the steady state value after 10 days of simulation, to ensure the sub-model closely resembled the full model. Parameters from the best-fitting D2FC2 model were used for the simulations.

$$Rate_{unbinding} = kd1d * [N.NFkBDNA] + ka2a * [N.IkBa_{steady-state}] [N.NFkBDNA]$$

References

1 Hatton, I. A. *et al.* The human cell count and size distribution. *Proceedings of the National Academy of Sciences* **120**, e2303077120, doi:10.1073/pnas.2303077120 (2023).

2 Hoesel, B. & Schmid, J. A. The complexity of NF-κB signaling in inflammation and cancer. *Molecular Cancer* **12**, 86, doi:10.1186/1476-4598-12-86 (2013).

3 Taniguchi, K. & Karin, M. NF-κB, inflammation, immunity and cancer: coming of age. *Nature Reviews Immunology* **18**, 309-324, doi:10.1038/nri.2017.142 (2018).

4 Staudt, L. M. Oncogenic activation of NF-kappaB. *Cold Spring Harb Perspect Biol* **2**, a000109, doi:10.1101/cshperspect.a000109 (2010).

5 Raj, A. & van Oudenaarden, A. Nature, nurture, or chance: stochastic gene expression and its consequences. *Cell* **135**, 216-226, doi:10.1016/j.cell.2008.09.050 (2008).

6 Elowitz, M. B., Levine, A. J., Siggia, E. D. & Swain, P. S. Stochastic gene expression in a single cell. *Science* **297**, 1183-1186, doi:10.1126/science.1070919 (2002).

7 Wen, J. D. *et al.* Following translation by single ribosomes one codon at a time. *Nature* **452**, 598-603, doi:10.1038/nature06716 (2008).

8 Livingston, N. M. *et al.* Bursting translation on single mRNAs in live cells. *Mol Cell* **83**, 2276-2289 e2211, doi:10.1016/j.molcel.2023.05.019 (2023).

9 Son, M., Wang, A. G., Keisham, B. & Tay, S. Processing stimulus dynamics by the NF-κB network in single cells. *Experimental & Molecular Medicine* **55**, 2531-2540, doi:10.1038/s12276-023-01133-7 (2023).

10 Micheau, O. & Tschopp, J. Induction of TNF receptor I-mediated apoptosis via two sequential signaling complexes. *Cell* **114**, 181-190 (2003).

11 Barnhart, B. C. & Peter, M. E. The TNF receptor 1: a split personality complex. *Cell* **114**, 148-150, doi:10.1016/s0092-8674(03)00561-0 (2003).

12 Laplantine, E. *et al.* NEMO specifically recognizes K63-linked poly-ubiquitin chains through a new bipartite ubiquitin-binding domain. *EMBO J* **28**, 2885-2895, doi:10.1038/emboj.2009.241 (2009).

13 Clark, K., Nanda, S. & Cohen, P. Molecular control of the NEMO family of ubiquitin-binding proteins. *Nat Rev Mol Cell Biol* **14**, 673-685, doi:10.1038/nrm3644 (2013).

14 Haas, T. L. *et al.* Recruitment of the linear ubiquitin chain assembly complex stabilizes the TNF-R1 signaling complex and is required for TNF-mediated gene induction. *Mol Cell* **36**, 831-844, doi:10.1016/j.molcel.2009.10.013 (2009).

15 Kim, A. H., Chiknas, P. M. & Lee, R. E. C. Ubiquitin: Not just a one-way ticket to the proteasome, but a therapeutic dial to fine-tune the molecular landscape of disease. *Clin Transl Med* **14**, e1769, doi:10.1002/ctm2.1769 (2024).

16 Tarantino, N. *et al.* TNF and IL-1 exhibit distinct ubiquitin requirements for inducing NEMO-IKK supramolecular structures. *J Cell Biol* **204**, 231-245, doi:10.1083/jcb.201307172 (2014).

17 Cruz, J. A. *et al.* A variable-gain stochastic pooling motif mediates information transfer from receptor assemblies into NF-kappaB. *Sci Adv* **7**, doi:10.1126/sciadv.abi9410 (2021).

18 Chen, Z. J. Ubiquitination in signaling to and activation of IKK. *Immunol Rev* **246**, 95-106, doi:10.1111/j.1600-065X.2012.01108.x (2012).

19 Israel, A. The IKK complex, a central regulator of NF-kappaB activation. *Cold Spring Harb Perspect Biol* **2**, a000158, doi:10.1101/cshperspect.a000158 (2010).

20 Nelson, D. E. *et al.* Oscillations in NF-κB Signaling Control the Dynamics of Gene Expression. *Science* **306**, 704-708, doi:doi:10.1126/science.1099962 (2004).

21 Ashall, L. *et al.* Pulsatile Stimulation Determines Timing and Specificity of NF-κB-Dependent Transcription. *Science* **324**, 242-246, doi:10.1126/science.1164860 (2009).

22 Cheng, Q. J. *et al.* NF-κB dynamics determine the stimulus specificity of epigenomic reprogramming in macrophages. *Science* **372**, 1349-1353, doi:doi:10.1126/science.abc0269 (2021).

23 Lee, R. E., Qasaimeh, M. A., Xia, X., Juncker, D. & Gaudet, S. NF-kappaB signalling and cell fate decisions in response to a short pulse of tumour necrosis factor. *Sci Rep* **6**, 39519, doi:10.1038/srep39519 (2016).

24 Mokashi, C. S., Schipper, D. L., Qasaimeh, M. A. & Lee, R. E. C. A System for Analog Control of Cell Culture Dynamics to Reveal Capabilities of Signaling Networks. *iScience* **19**, 586-596, doi:10.1016/j.isci.2019.08.010 (2019).

25 Thiemicke, A., Jashnsaz, H., Li, G. & Neuert, G. Generating kinetic environments to study dynamic cellular processes in single cells. *Sci Rep* **9**, 10129, doi:10.1038/s41598-019-46438-8 (2019).

26 Dettinger, P. *et al.* Automated Microfluidic System for Dynamic Stimulation and Tracking of Single Cells. *Anal Chem* **90**, 10695-10700, doi:10.1021/acs.analchem.8b00312 (2018).

27 Lee, R. E. C., Qasaimeh, M. A., Xia, X., Juncker, D. & Gaudet, S. NF-κB signalling and cell fate decisions in response to a short pulse of tumour necrosis factor. *Scientific Reports* **6**, 39519, doi:10.1038/srep39519 (2016).

28 Thiemicke, A. & Neuert, G. Kinetics of osmotic stress regulate a cell fate switch of cell survival. *Sci Adv* **7**, doi:10.1126/sciadv.abe1122 (2021).

29 Son, M. *et al.* NF-kappaB responds to absolute differences in cytokine concentrations. *Sci Signal* **14**, doi:10.1126/scisignal.aaz4382 (2021).

30 Blum, Y. *et al.* Temporal perturbation of ERK dynamics reveals network architecture of FGF2/MAPK signaling. *Mol Syst Biol* **15**, e8947, doi:10.15252/msb.20198947 (2019).

31 Ryu, H. *et al.* Frequency modulation of ERK activation dynamics rewires cell fate. *Mol Syst Biol* **11**, 838, doi:10.15252/msb.20156458 (2015).

32 Lee, Robin E. C., Walker, Sarah R., Savery, K., Frank, David A. & Gaudet, S. Fold Change of Nuclear NF-κB Determines TNF-Induced Transcription in Single Cells. *Molecular Cell* **53**, 867-879, doi:https://doi.org/10.1016/j.molcel.2014.01.026 (2014).

33 Zhang, Q. *et al.* NF-κB Dynamics Discriminate between TNF Doses in Single Cells. *Cell systems* **5**, 638-645.e635, doi:10.1016/j.cels.2017.10.011 (2017).

34 Kellogg, R. A., Tian, C., Lipniacki, T., Quake, S. R. & Tay, S. Digital signaling decouples activation probability and population heterogeneity. *Elife* **4**, e08931, doi:10.7554/eLife.08931 (2015).

35 Hazuda, D. J., Lee, J. C. & Young, P. R. The kinetics of interleukin 1 secretion from activated monocytes. Differences between interleukin 1 alpha and interleukin 1 beta. *J Biol Chem* **263**, 8473-8479 (1988).

36 Kudo, S., Mizuno, K., Hirai, Y. & Shimizu, T. Clearance and tissue distribution of recombinant human interleukin 1 beta in rats. *Cancer Res* **50**, 5751-5755 (1990).

37 Chapman, P. B. *et al.* Clinical pharmacology of recombinant human tumor necrosis factor in patients with advanced cancer. *J Clin Oncol* **5**, 1942-1951, doi:10.1200/JCO.1987.5.12.1942 (1987).

38 Oyler-Yaniv, J. *et al.* Catch and Release of Cytokines Mediated by Tumor Phosphatidylserine Converts Transient Exposure into Long-Lived Inflammation. *Mol Cell* **66**, 635-647 e637, doi:10.1016/j.molcel.2017.05.011 (2017).

39 Hoffmann, A., Levchenko, A., Scott, M. L. & Baltimore, D. The IκB-NF-κB Signaling Module: Temporal Control and Selective Gene Activation. *Science* **298**, 1241-1245, doi:doi:10.1126/science.1071914 (2002).

40 Kennedy, J. & Eberhart, R. in *Proceedings of ICNN'95 - International Conference on Neural Networks*. 1942-1948 vol.1944.

41 Natoli, G., Saccani, S., Bosisio, D. & Marazzi, I. Interactions of NF-kappaB with chromatin: the art of being at the right place at the right time. *Nat Immunol* **6**, 439-445, doi:10.1038/ni1196 (2005).

42 Martone, R. *et al.* Distribution of NF-kappaB-binding sites across human chromosome 22. *Proc Natl Acad Sci U S A* **100**, 12247-12252, doi:10.1073/pnas.2135255100 (2003).

43 Brignall, R., Moody, A. T., Mathew, S. & Gaudet, S. Considering Abundance, Affinity, and Binding Site Availability in the NF-kappaB Target Selection Puzzle. *Front Immunol* **10**, 609, doi:10.3389/fimmu.2019.00609 (2019).

44 Zhao, B. *et al.* The NF-kappaB genomic landscape in lymphoblastoid B cells. *Cell Rep* **8**, 1595-1606, doi:10.1016/j.celrep.2014.07.037 (2014).

45 Link, V. M. *et al.* Analysis of Genetically Diverse Macrophages Reveals Local and Domain-wide Mechanisms that Control Transcription Factor Binding and Function. *Cell* **173**, 1796-1809 e1717, doi:10.1016/j.cell.2018.04.018 (2018).

46 Stormberg, T., Filliaux, S., Baughman, H. E. R., Komives, E. A. & Lyubchenko, Y. L. Transcription factor NF-κB unravels nucleosomes. *Biochim Biophys Acta Gen Subj* **1865**, 129934, doi:10.1016/j.bbagen.2021.129934 (2021).

47 Lone, I. N. *et al.* Binding of NF-kappaB to nucleosomes: effect of translational positioning, nucleosome remodeling and linker histone H1. *PLoS Genet* **9**, e1003830, doi:10.1371/journal.pgen.1003830 (2013).

48 Sen, S., Cheng, Z., Sheu, K. M., Chen, Y. H. & Hoffmann, A. Gene Regulatory Strategies that Decode the Duration of NFkappaB Dynamics Contribute to LPS-versus TNF-Specific Gene Expression. *Cell Syst* **10**, 169-182 e165, doi:10.1016/j.cels.2019.12.004 (2020).

49 Hansen, J. L., Loell, K. J. & Cohen, B. A. A test of the pioneer factor hypothesis using ectopic liver gene activation. *Elife* **11**, doi:10.7554/eLife.73358 (2022).

50 Christman, J. K. 5-Azacytidine and 5-aza-2'-deoxycytidine as inhibitors of DNA methylation: mechanistic studies and their implications for cancer therapy. *Oncogene* **21**, 5483-5495, doi:10.1038/sj.onc.1205699 (2002).

51 Werner, S. L., Barken, D. & Hoffmann, A. Stimulus specificity of gene expression programs determined by temporal control of IKK activity. *Science* **309**, 1857-1861, doi:10.1126/science.1113319 (2005).

52 Bergqvist, S. *et al.* Kinetic enhancement of NF-kappaBxDNA dissociation by IkappaBalpha. *Proc Natl Acad Sci U S A* **106**, 19328-19333, doi:10.1073/pnas.0908797106 (2009).

53 Grell, M., Wajant, H., Zimmermann, G. & Scheurich, P. The type 1 receptor (CD120a) is the high-affinity receptor for soluble tumor necrosis factor. *Proc Natl Acad Sci U S A* **95**, 570-575, doi:10.1073/pnas.95.2.570 (1998).

54 Mizel, S. B., Kilian, P. L., Lewis, J. C., Paganelli, K. A. & Chizzonite, R. A. The interleukin 1 receptor. Dynamics of interleukin 1 binding and internalization in T cells and fibroblasts. *J Immunol* **138**, 2906-2912 (1987).

55 Watanabe, N. *et al.* Continuous internalization of tumor necrosis factor receptors in a human myosarcoma cell line. *J Biol Chem* **263**, 10262-10266 (1988).

56 Werner, S. L. *et al.* Encoding NF-kappaB temporal control in response to TNF: distinct roles for the negative regulators IkappaBalpha and A20. *Genes & development* **22**, 2093-2101, doi:10.1101/gad.1680708 (2008).

57 Siggers, T. *et al.* Principles of dimer-specific gene regulation revealed by a comprehensive characterization of NF-kappaB family DNA binding. *Nat Immunol* **13**, 95-102, doi:10.1038/ni.2151 (2011).

58 Weigelin, B. *et al.* Cytotoxic T cells are able to efficiently eliminate cancer cells by additive cytotoxicity. *Nat Commun* **12**, 5217, doi:10.1038/s41467-021-25282-3 (2021).

59 Weigelin, B. & Friedl, P. T cell-mediated additive cytotoxicity - death by multiple bullets. *Trends Cancer* **8**, 980-987, doi:10.1016/j.trecan.2022.07.007 (2022).

60 Tian, B., Nowak, D. E. & Brasier, A. R. A TNF-induced gene expression program under oscillatory NF-kappaB control. *BMC Genomics* **6**, 137, doi:10.1186/1471-2164-6-137 (2005).

61 Wolf, B. K. *et al.* Cooperation of chromatin remodeling SWI/SNF complex and pioneer factor AP-1 shapes 3D enhancer landscapes. *Nat Struct Mol Biol* **30**, 10-21, doi:10.1038/s41594-022-00880-x (2023).

62 Vierbuchen, T. *et al.* AP-1 Transcription Factors and the BAF Complex Mediate Signal-Dependent Enhancer Selection. *Mol Cell* **68**, 1067-1082 e1012, doi:10.1016/j.molcel.2017.11.026 (2017).

63 Guo, Y., Kowalczyk, G. J. & Lee, R. E. C. Label and quantify mRNA molecules in live cell experiments using SunRISER and dNEMO. *STAR Protoc* **3**, 101630, doi:10.1016/j.xpro.2022.101630 (2022).

64 Kowalczyk, G. J. *et al.* dNEMO: a tool for quantification of mRNA and punctate structures in time-lapse images of single cells. *Bioinformatics* **37**, 677-683, doi:10.1093/bioinformatics/btaa874 (2020).

939 **Acknowledgements**

940 We thank other members of the Lee lab and colleagues in the Department of Computational

941 and Systems Biology for many helpful discussions. This work was supported by generous

942 funding to R.E.C.L. from NIH grant R35-GM119462.

Figure legends

Fig. 1: NEMO features determine same-cell NF-kB responses to a single cytokine pulse. **A.** Schematic of a two-inlet, one outlet microfluidic chip with fluid flow from left to right. Inlet 1 (I1) contains a mixture of cytokine, dye, and medium, while inlet 2 (I2) contains only media. The fluorescent dye is used exclusively to establish the position of the cytokine-containing stream. U2OS cells are cultured and imaged within the central cell culture channel. On average, 22 cells were imaged for each condition. **B.** Image of the custom gravity pump. Inlet reservoirs I1 and I2 are connected to the orange basins and the outlet connected to the gray basin. The gravity pump dynamically adjusts the relative heights of the basins to control fluid flow. When the I1 basin is positioned lower than I2, cells are exposed to media only (top) and when I1 is higher, cells are exposed to cytokine (bottom). **C.** Time-lapse images of CRISPR-modified U2OS cells lines containing fluorescent protein fusions from their endogenous loci (left; see also Supplementary Movie 1). Quantification of upstream activated receptor complex measured through the formation and tracking of single EGFP-NEMO puncta (top). Quantification of downstream activation of the NF-κB (RelA) transcriptional system calculated by the fold change of mCh-RelA fluorescence in the nucleus (bottom). **D.** Single cell time-courses for EGFP-NEMO spot numbers and nuclear mCh-RelA nuclear fold change in response to a single pulse of IL-1 at 10 ng/ml with varying pulse durations. Light-colored trajectories represent individual cells, while bold trajectories represent the average response. **E.** The area under the curve (AUC) for the number of IL-1 induced spots (left) and the fold change of nuclear RelA (right) increases with pulse duration. **F.** Same-cell correlations from dual-reporter cells show the aggregate AUC of activated receptor

965 complexes and downstream transcriptional activity display a monotonic relationship
966 (Spearman ρ = 0.85).
967
968 **Fig. 2: NF-kB responses to a dose-conserving cytokine pulse train are enhanced.**
969 **A.** Single cell time-courses for EGFP-NEMO spot numbers and nuclear mCh-RelA nuclear
970 fold change responses to multiple short pulses. Single 6- and 15-minute pulses are shown
971 as reference points, representing equivalent and greater than twice the total cytokine
972 exposure, respectively, compared to the multiple short pulses (yellow highlighted
973 conditions; see also Supplementary Movies 1 and 2). On average, 20 single cells were
974 imaged per condition. **B.** The area under the curve (AUC) analysis of NEMO spot numbers
975 (left) shows no significant difference between single and multiple pulse stimulation
976 patterns. For comparison, the single 6- and 15-minute pulses do show a significant
977 difference (left). By contrast, the AUC for nuclear RelA fold change indicates a significant
978 difference between single and multiple pulse stimulation patterns (right). Median and
979 interquartile ranges are shown. **P<10^{-2}, student's t-test. **C.** The aggregate AUC of activated
980 receptor complexes and downstream transcriptional activity is not monotonic when
981 responses to multiple short pulses are combined.
982
983 **Fig. 3: Temporal features of NEMO spot numbers correlate with NF-kB and zero-order**
984 **export kinetics following a cytokine pulse train.**
985 **A.** Schematic of a typical NEMO spot trajectory highlighting features for the 'time to
986 maximum' (t_{max}) and 'adaptation time' (t_{adapt}). **B.** Boxplots showing t_{max} for single-cell

trajectories under 6-minute single and multi-pulse stimulation. **C.** Boxplots showing t_{adapt} for single-cell trajectories under 6-minute single and multi-pulse stimulation. **D.** Schematic of a typical nuclear RelA fold change trajectory highlighting the max fold change and the area under the curve (AUC). Additionally, examples for zero-order and first-order kinetics are illustrated for nuclear RelA export. **E.** Same cell correlations for time-courses of nuclear RelA exit rates scores and the t_{max} of NEMO. **F.** Same cell correlations for time-courses of nuclear RelA exit rates scores and the t_{adapt} of NEMO (min)

Fig. 4: A model with DNA-binding and chromatin remodeling recapitulates emergent properties of average cellular responses to dynamic stimuli.

A. Schematic of the mechanistic model fitting strategy. As input, the model uses experimental averages of EGFP-NEMO time-courses from four conditions, chosen to tune the model to the emergent property. Simulated NF-kB responses are compared against experimental results and used as a cost function for particle swarm optimization (PSO). **B.** Results of PSO from 500 replicates for each model architecture. Each model parameterization is evaluated based on the sum of squared error (SSE) to the 4 training conditions (x-axis), to the SSE of averages from the 5 validation conditions not used for PSO (y-axis), and emergent property error score (colorbar). D2FC optimized models were limited to the quadrant highlighted in pink. The red star indicates the overall best $D2FC^2$ model.

Fig. 5: $D2FC^2$ accurately predicts NF-kB responses using single cell CI data as inputs

A. Simulated single-cell NF-kB predictions using the best-performing $D2FC^2$ model using

single-cell EGFP-NEMO as model inputs. **B and C.** Boxplots comparing the simulated and experimental AUC of nuclear RelA for single-pulse (B) and multi-pulse (C) dosing schedules. Between experiments and D2FC^2 simulations, the model shows remarkable similarity where only one condition has a statistically distinct difference (marked with *; $p < 0.05$, student's t-test). **D.** Proportion of single-cell predictions classified as excellent, high, or low quality (see also, Supplementary Fig. 7) compared to experimental data across different dosing schemes for the best-performing model (left). Overall performance of the top 10 models in predicting single-cell trajectories aggregated across all experimental conditions (right). See also Supplementary Table 3.

Fig. 6: D2FC^2 accurately predicts cytokine-induced NF-kB responses following exposure to hypomethylating azacytidine.

A. Simulated estimate of baseline nuclear RelA (relative to original) in response increasing basal chromatin opening. **B.** Simulated nuclear RelA (fold change) using the average EGFP-NEMO time course from a single 6-min pulse as an input. Different colors represent indicated amounts of basal chromatin opening. **C.** Experimental measurements of basal nuclear RelA of cells exposed to 5 uM of Azacytidine for 3 and 6 days, respectively. **D.** Single-cell trajectories of nuclear RelA fold change for cells exposed to a single 6-minute pulse of IL-1 following azacytidine exposure for 3 or 6 days (top and bottom, respectively). Bold lines represent the average trajectory, and the shaded region is +/- 1 standard deviation. On average 26 cells were imaged in each condition. See also Supplementary Fig. 8.

Fig. 7: Features of NF-kB responses show different sensitivities to features of CI

A. Schematic illustrating how NEMO features encoded by temporal stimulation impacts binding site availability and the duration of NF-κB retention. **B.** Simulated IKK trajectories varying the peak of NEMO numbers (top, peak), adaptation time of NEMO numbers (middle, t_{adapt}) independently. Combined features are used to generate simulated time-courses that scan the encoding space of NEMO puncta (bottom). **C.** Heatmap of: simulated peak nuclear RelA (fold change) with varying peak NEMO and adaptation times (top-left); Nuclear RelA export scores for simulated responses, where positive values indicate increasingly zero-order scores and negative values indicating the strength of first-order scores (top-right); Relative chromatin permissiveness, where higher values represent more open chromatin (bottom-left); and, results from a sub-model used to simulate the steady-state fraction of free nuclear NF-kB changes with overall nuclear NF-kB and chromatin permissiveness (bottom-right).

Figure 1

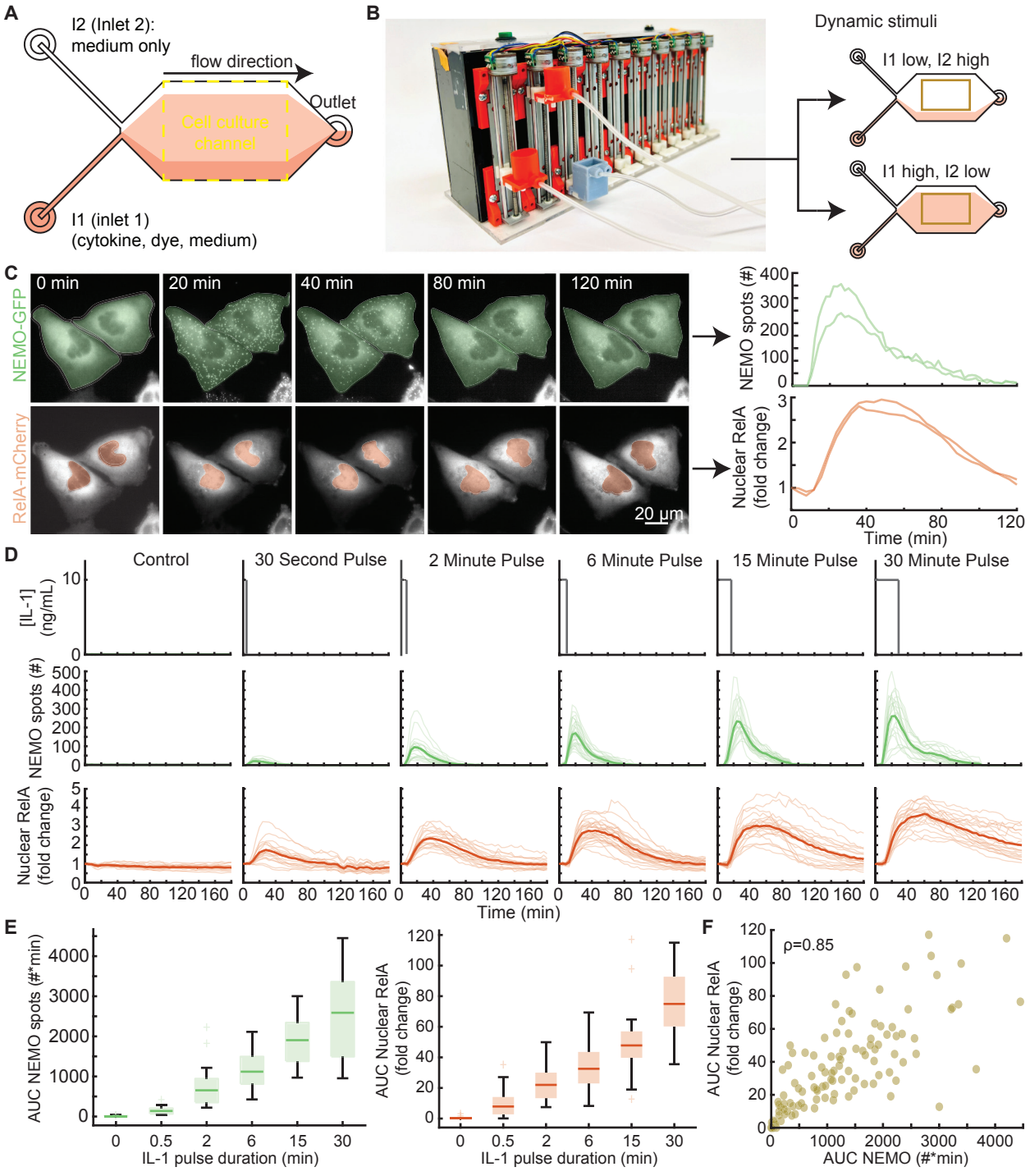

Figure 2

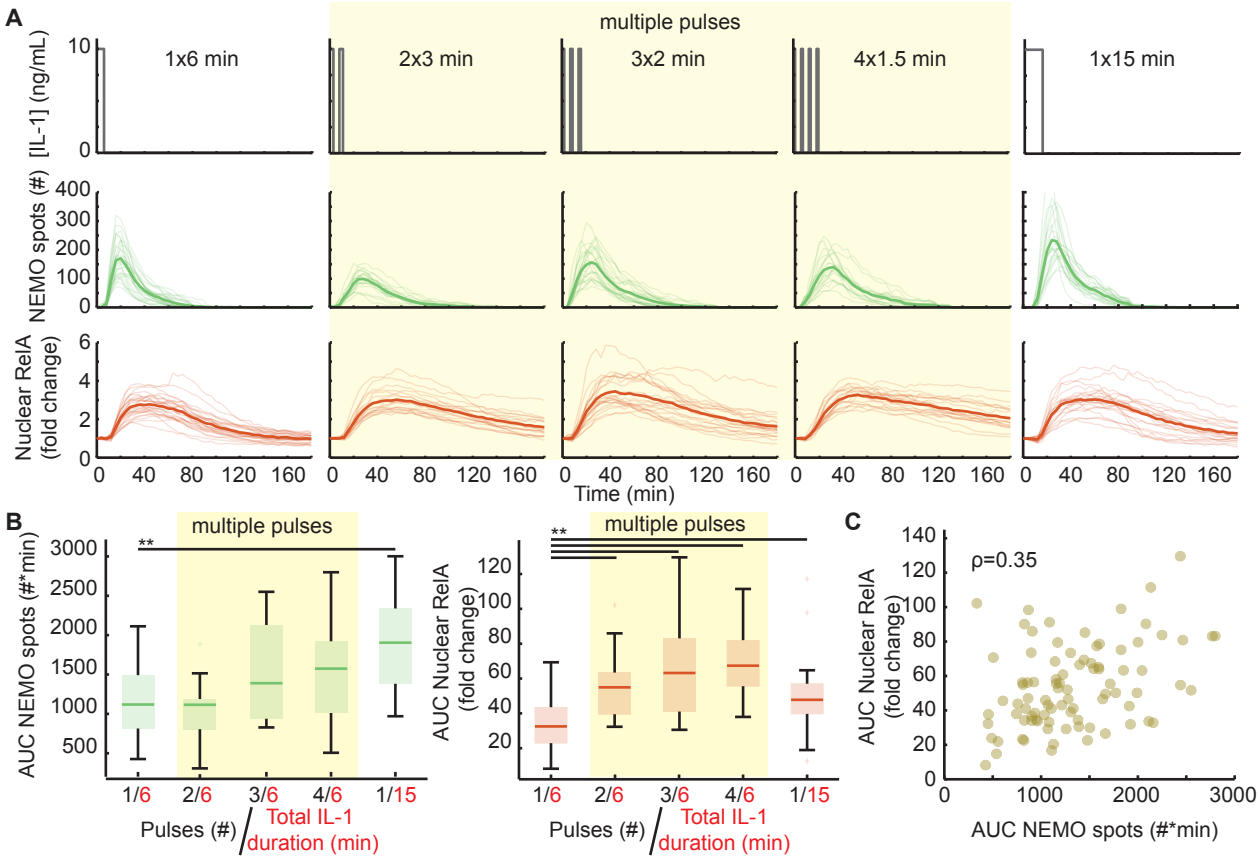

Figure 3

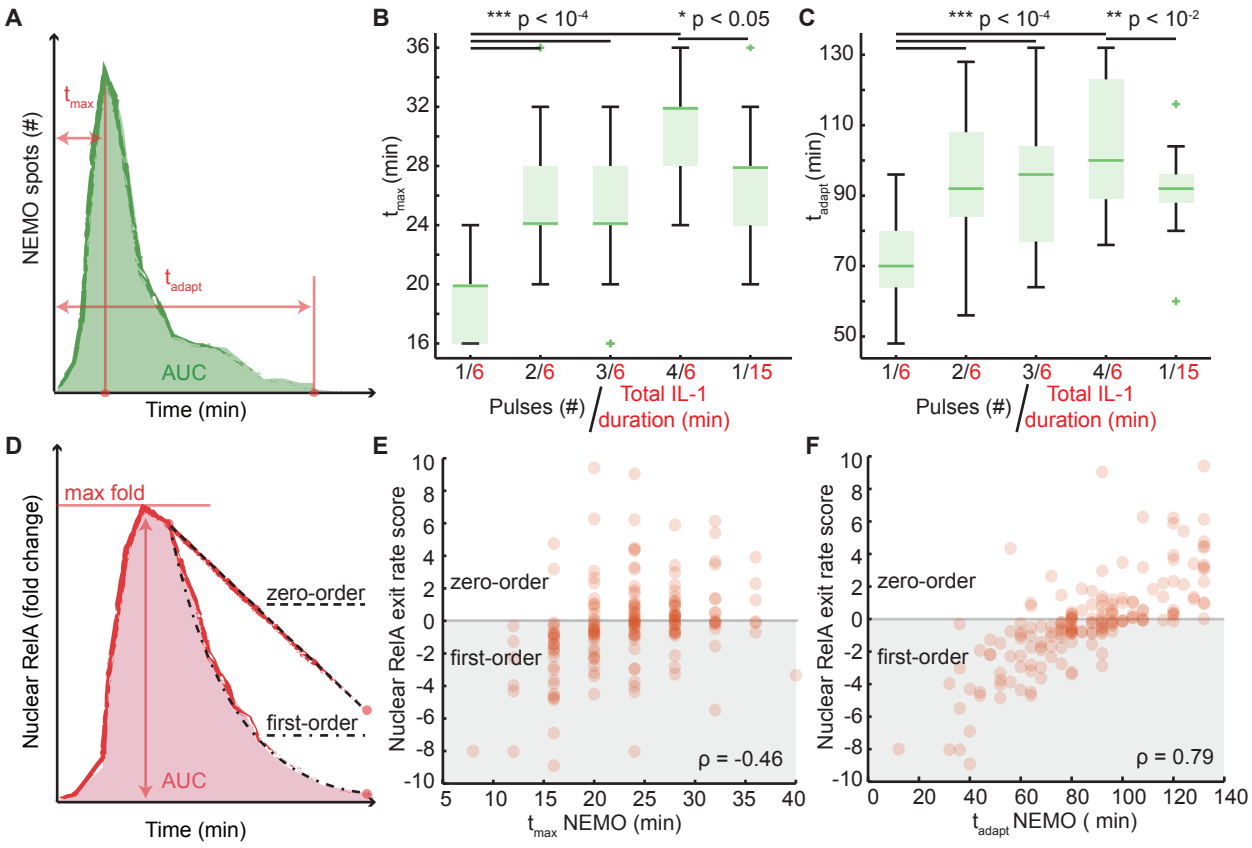

Figure 4

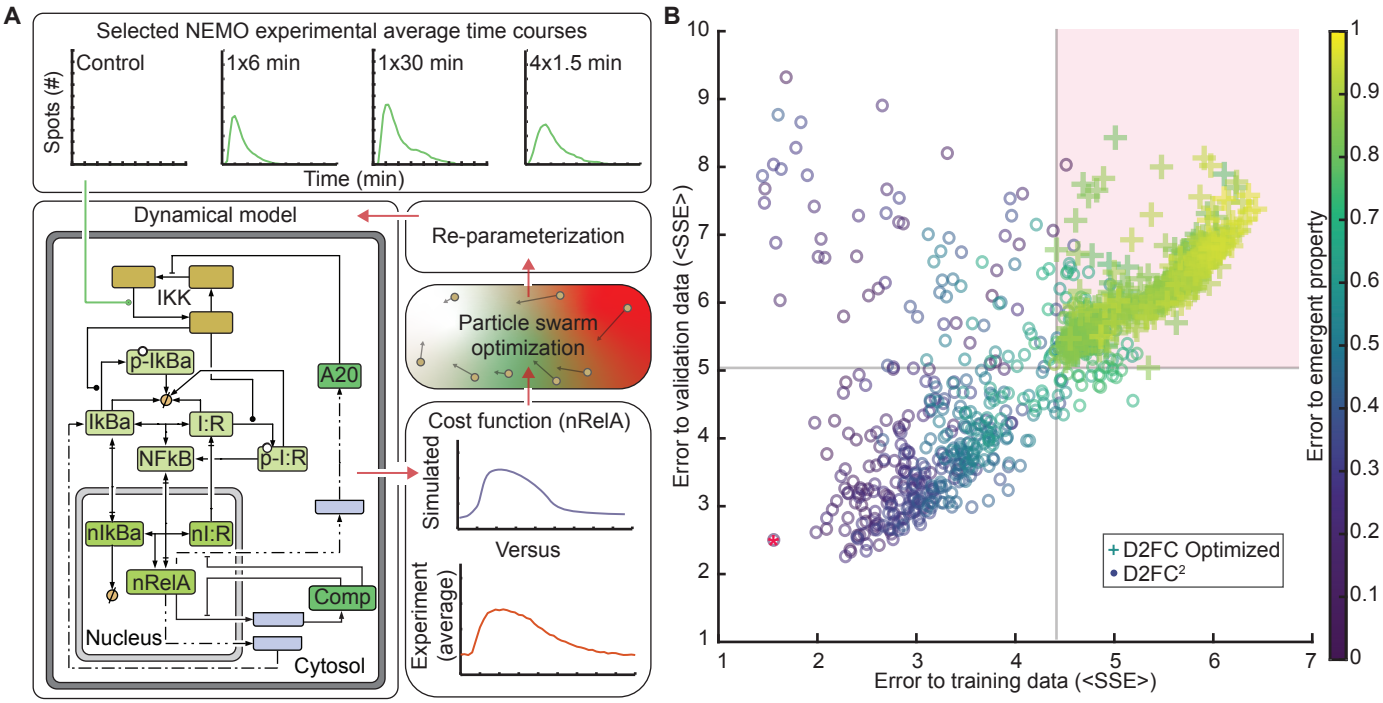

Figure 5

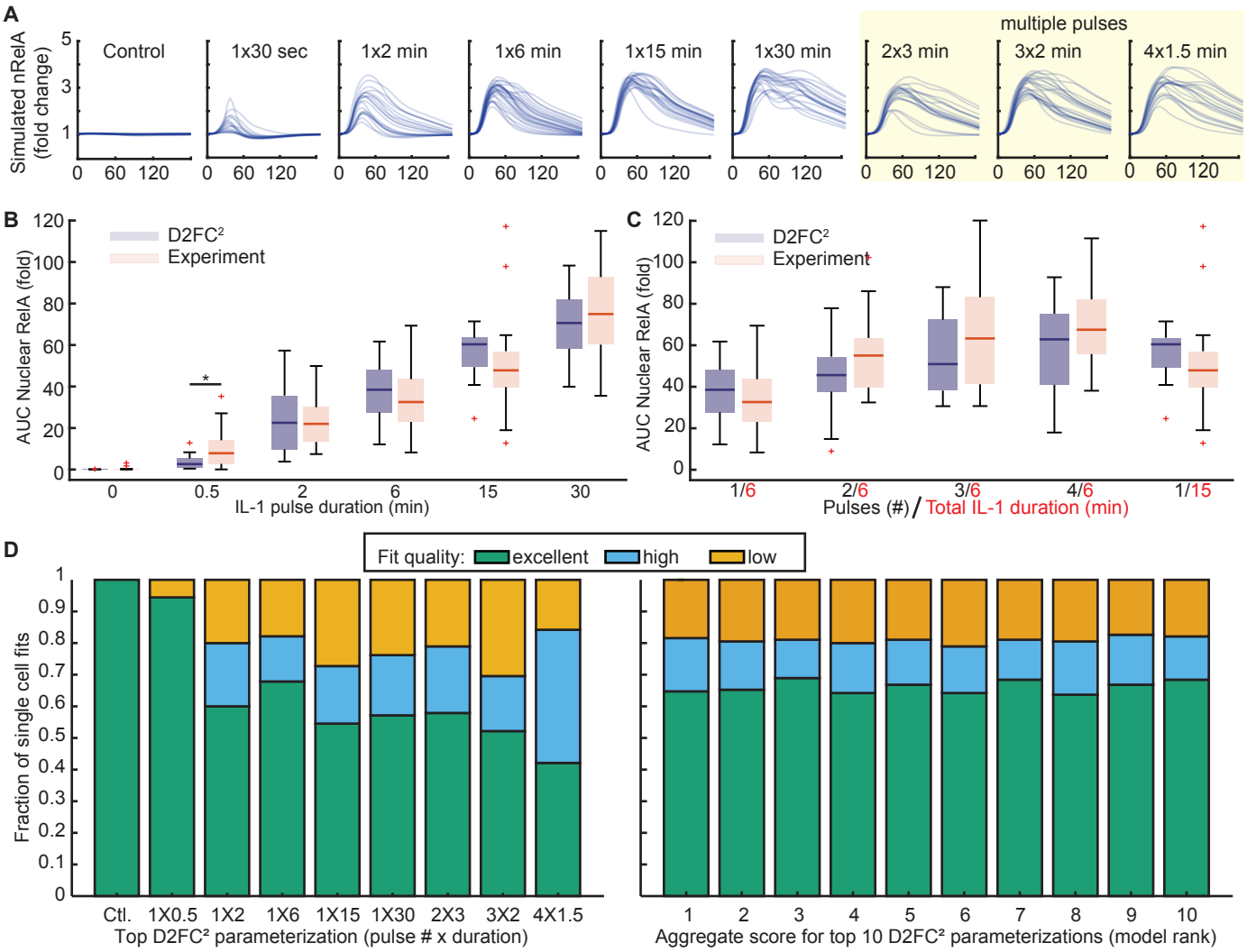

Figure 6

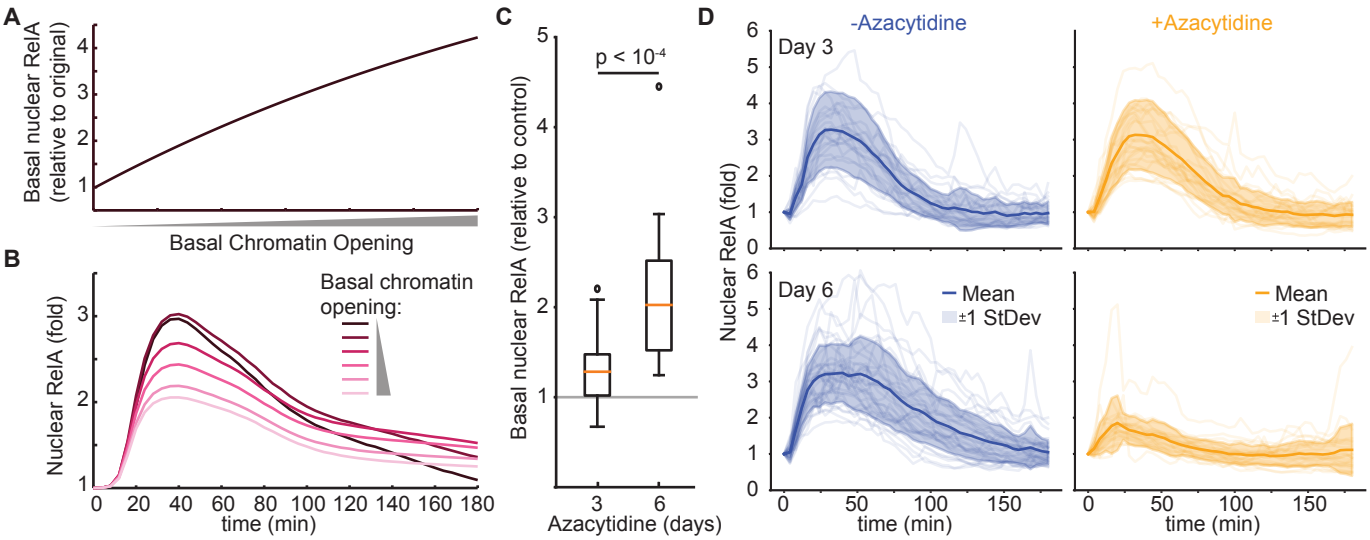

Figure 7